

This thesis is dedicated
to
my beloved
Ammu and Sister

Statement by author

This dissertation has been presented to meet the partial requirements for the attainment of an advanced degree at the University of North Bengal (NBU) and has been deposited in the library for lending under the regulations of the NBU. Brief excerpts from this dissertation may be used without special permission, provided proper acknowledgment of the source is made. Requests for permission to reproduce or quote extensively from this manuscript, in whole or in part, may be granted by the authorized personnel of NBU if deemed beneficial for academic purposes. Otherwise, permission must be sought from the author.

Ziaur Rahman

Declaration

I hereby declare that this thesis entitled "**Photophysical and sensorial behavior of different chromophoric systems comprising electron donor-acceptor units**" embodies my original research work, conducted under the supervision of Dr. Sudhir Kumar Das, at the Department of Chemistry, University of North Bengal.

The work presented in this thesis results from my independent investigation and reflects my efforts and understanding of the subject matter. All the data, results, and conclusions presented in this document are based on genuine research findings and have not been previously submitted for any other degree or qualification at this or any other institution.

I affirm that the content of this thesis is the result of my research work and is presented with utmost honesty and integrity.

Ziaur Rahman

Ziaur Rahman

Department of Chemistry

University of North Bengal

Darjeeling-734013

West Bengal, India

Date: 05.12.2023

UNIVERSITY OF NORTH BENGAL

Dr. Sudhir Kumar Das, Ph. D
Assistant Professor
Department of Chemistry
North Bengal University
Darjeeling, 734013



Email: sudhirkumardas@nbu.ac.in
Mobile: 91-8016884965

‘समानो मन्त्र समितिः समानी’

Accredited by NAAC with Grade B**

Certificate

I certify that Mr. Ziaur Rahman has prepared the thesis entitled “**Photophysical and sensorial behavior of different chromophoric systems comprising electron donor-acceptor units**” for the award of Ph.D. degree of the University of North Bengal, under my guidance. He has carried out the research work at the Department of Chemistry, University of North Bengal.

Sudhir 05/12/2023
Dr. Sudhir Kumar Das
Assistant Professor
Department of Chemistry
North Bengal University
Darjeeling, 734013
West Bengal, India

Dr. Sudhir Kumar Das
Assistant Professor
Department of Chemistry
University of North Bengal
Darjeeling - 734013, India

Anti-plagiarism report



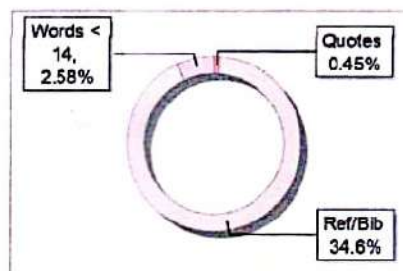
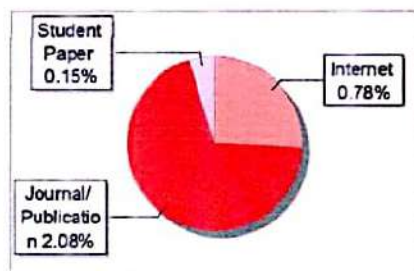
The Report is Generated by DrillBit Plagiarism Detection Software

Submission Information

Author Name: Ziaur Rahman
Title: Photophysical and sensorial behavior of different chromophoric systems comprising electron donor-acceptor units
Paper Submission ID: 1119764
Submitted by: nbuplg@nbu.ac.in
Submission Date: 2023-11-21 13:55:34
Total Pages: 120
Document type: Thesis

Result Information

Similarity 3 %



Exclude Information

Quotes: Excluded
References/Bibliography: Excluded
Sources: Less than 14 Words Similarity: Not Excluded
Excluded Source: 2 %
Excluded Phrases: Not Excluded

A Sample QR - code can be Scan Download/View PDF File



S.K. Das
05/12/2023
Dr. Sudhir Kumar Das
Assistant Professor
Department of Chemistry
University of North Bengal
Darjeeling - 734013, India

Ziaur Rahman
05/12/2023

Preface

It is with great pleasure and a sense of profound accomplishment that I present this thesis, titled "**Photophysical and sensorial behavior of different chromophoric systems comprising electron donor-acceptor units**," as a culmination of my journey towards obtaining a Doctor of Philosophy (Ph.D.) degree in Chemistry. This research work reflects the dedicated efforts and unyielding passion that have driven me throughout my academic pursuit.

My registration for the Ph.D. program at the University of North Bengal commenced on 2nd January 2020, vide letter no. Ph.D./Chem. (1723)/627/R-2023, under the esteemed guidance of Dr. Sudhir Kumar Das. I embarked on this scholarly endeavor to explore the intriguing realm of photophysical and sensorial properties of diverse chromophoric systems that incorporate electron donor-acceptor units.

The motivation behind this research stemmed from the ever-growing interest in understanding the interactions between electron donor and acceptor moieties within molecular systems and their profound influence on photophysical phenomena and sensorial responses. These chromophoric systems exhibit intriguing properties that have the potential for various applications, such as organic photovoltaics, light-emitting devices, and molecular sensors. Unlocking the underlying mechanisms governing their behavior and exploring their potential in real-world applications has driven this investigation.

I am deeply indebted to my esteemed supervisor, Dr. Sudhir Kumar Das, whose profound knowledge, expertise, and guidance have been instrumental in shaping the direction of this research. His constant encouragement, valuable insights, and constructive feedback have been the guiding beacons that illuminated my path during moments of uncertainty.

I also extend my heartfelt gratitude to the Department of Chemistry at the University of North Bengal for providing a nurturing academic environment and access to state-of-the-art facilities, which proved essential in conducting this research.

Acknowledgments

I sincerely thank **Dr. Sudhir Kumar Das**, my supervisor, for his invaluable scientific assistance and unwavering support throughout my research. His extensive knowledge and passion for science have been a constant source of inspiration, motivating me to excel in the laboratory. I feel privileged to have worked with him and appreciate his patience in critically reviewing this thesis.

I sincerely thank my thesis committee members for their valuable suggestions and guidance throughout my research work. I would also like to acknowledge the support of **Prof. B. Sinha**, Head of the Department of Chemistry at NBU. I am thankful to all the Department of Chemistry faculty members for their support and encouragement and for serving as role models for my academic career.

I wish to acknowledge the invaluable contributions of my colleagues **Manas, Najmin, Sabbir, Pallabi, Tuhina, Madan**, and **Jyoti**, with whom working in the lab has been a joyous experience. I am also grateful to all my friends at NBU for their constant support and companionship, which have made my life more pleasant.

I thank the Science and Engineering Board (**SERB**), New Delhi, for the financial support and the Department of Science and Technology-Fund for Improvement of Science and Technology Infrastructure (**DST-FIST**) for providing research infrastructure.

Lastly, I am deeply indebted to several individuals who have motivated, encouraged, and supported me in all my pursuits. I extend my heartfelt gratitude to my parents, whose unwavering support and encouragement have been instrumental in all my achievements.

Mr. Ziaur Rahman
Research Scholar
Department of Chemistry
University of North Bengal
Darjeeling-734013, INDIA

Glossary of acronyms

EDA	Electron donor-acceptor
ET	Electron transfer
EDG	Electron donating group
EWG	Electron withdrawing group
HOMO	Highest occupied molecular orbital
LUMO	Lowest unoccupied molecular orbital
LMCT	Ligand to metal charge transfer
MLCT	Metal to ligand charge transfer
AIE	Aggregation-induced emission
ESIPT	Excited-state intramolecular proton transfer
PET	Photoinduced electron transfer
ICT	Intramolecular charge transfer
TICT	Twisted intramolecular charge transfer
FRET	Forster resonance energy transfer
ISC	Intersystem crossing
ACQ	Aggregation-caused quenching
AIEE	Aggregation-induced fluorescence enhancement
HPS	Hexaphenylsilole
RIR	Restriction of intramolecular rotation
NAC	Nitro-aromatic compound
SERS	Surface-enhanced resonance spectroscopy
MOF	Metal-organic framework
D	Donor
A	Acceptor
BSSS	Binding site signaling subunit
TMS	Tetramethylsilane
DMSO-d₆	Deuterated dimethyl sulfoxide
HRMS	High-resolution mass spectra
AcOH	Acetic acid
TFA	Trifluoroacetic acid
TEA	Triethylamine
LOD	Limit of detection

INH	INHIBIT
IMP	IMPLICATION
F⁻	Fluoride
ACN	Acetonitrile
HSO₄⁻	Hydrogen sulfate
TBA	Tetrabutylammonium
DFT	Density functional theory
TD-DFT	Time-dependent density functional theory
CPCM	Conductor-like polarizable continuum model
WHO	World Health Organization
AcO⁻	Acetate
B-H	Benesi–Hildebrand
R²	Regression coefficient
FMO	Frontier Molecular Orbital
Al³⁺	Aluminium
FAO	Joint Expert Committee on Food Additive
PA	Picric acid
NAC	Nitro aromatic compound
SERS	Surface-enhanced Raman spectroscopy
IMS	Ion-mobility spectrometry
GC	Gas chromatography
FT-IR	Fourier transform infrared
TCSPC	Time-correlated single-photon counting
PPD	Photon Counting Detector
IRF	Instrument response function
HADF	Human Adult Dermal Fibroblast
S-V	Stern-Volmer
TNT	2, 4, 6-trinitrotoluene
DNT	2, 4-dinitrotoluene
4-NA	4-nitro aniline
2-NP	2-nitrophenol
4-NP	4-nitrophenol
DNP	2,4-dinitrophenol

TLC	Thin layer chromatography
IL	Ionic liquid
GUMBOS	Group of uniform materials based on organic salts
PbNa	Sodium of Pyrene butyric acid
[TTP]⁺Cl⁻	Trihexyltetradecylphosphonium chloride
NMR	Nuclear magnetic resonance
DSC	Differential scanning calorimetry
DLS	Dynamic light scattering
SEM	Scanning electron microscopic
THF	Tetrahydrofuran
CWA	Chemical warfare agent
GB	Sarin
GD	Soman
GA	Tabun
OP	Organophosphorus
IP	Inorganophosphorus
DCP	Diethylchlorophosphate
DCNP	Diethylcyanophosphonate
DMMP	Dimethylmethylphosphate
TIMEP	Tetra iso-propyl methylene diphosphonate
TMP	Tri methyl phosphate
NaH₂PO₄	Monosodium phosphate
Na₂HPO₄	Di sodium phosphate
Na₃PO₄	Tri sodium phosphate
HCl	Hydrochloric acid
TEP	Tri ethyl phosphate
POCl₃	Phosphoryl chloride
T₂CP	Tris(2-chloroethyl) phosphate
BA	Benzyl acetone
MCE	Mercaptoethanol
BB	Benzyl bromide
2CPS	2-chloroethyl phenyl sulfide
2CES	2-chloroethyl ethyl sulfide

TA	Thioacetic acid
OPD	O-phenylenediamine
HPLC	High-performance liquid chromatography
PCM	Polarizable continuum model
SCRF	Self-consistent reaction field
m_p	Melting point

List of figures

Figures	Page No.
Figure-1.1. Schematic demonstration of chemosensor (a) interaction of “ A ” with analyte; (b) interaction of “ D ” with analyte.	3
Figure-1.2. Illustrative demonstration of the effect of binding of cation on D-π-A system and the UV-visible spectrum.	5
Figure-1.3. A diagram illustrating a sensor that undergoes alterations in photophysical properties upon detecting an analyte.	7
Figure-1.4. Schematic depiction of binding of the fluorophore.	7
Figure-1.5. The PET process is depicted schematically	9
Figure-1.6. Schematic illustration of reductive PET.	9
Figure-1.7. (a) Cation recognition based on fluorescent ICT sensors (Interact with “ D ” group) and (b) Cation recognition based on fluorescent ICT sensors (Interact with “ A ” group).	10
Figure-1.8. Schematic diagram showing paramagnetic fluorescence quenching.	11
Figure-1.9. Schematic representation of the FRET process.	11
Figure-1.10. Mechanism of ESIPT process.	13
Figure-1.11. Pictorial representations of AIE.	14
Figure-1.12. Schematic representation of the BSSS approach.	17
Figure-1.13. The displacement strategy is depicted schematically.	18
Figure-1.14. The chemodosimeter approach is depicted schematically.	18
Figure-1.15. Illustrates the fundamental schematics detailing diverse detection mechanisms employed for nerve agents. (a) indicator-spacer-receptor configuration, (b) amino phosphorylation of sensors, (c) phosphorylation and dephosphorylation dynamics, (d) intramolecular cyclization upon hydroxyl phosphorylation, and (e) optical detection of hydrolyzed nerve agent products, namely F^- , CN^- , and thiols.	20
Figure-2.1. 1H NMR spectra BPP in DMSO- d_6 .	30
Figure-2.2. ^{13}C NMR spectra of BPP in DMSO- d_6 .	31
Figure-2.3. IR spectra of BPP .	31
Figure-2.4. High-resolution mass spectra of BPP .	32

Figure-2.5.	(a, b) UV-visible absorption spectral change of BPP due to the addition of TFA and AcOH in ACN, respectively, and (c, d) display the change in absorbance values of BPP with the change in acid concentration.	34
Figure-2.6.	Visual color change of BPP in the presence of TFA in ACN.	34
Figure-2.7.	Frontier molecular orbital for BPP , BPP(NHC) systems.	36
Figure-2.8.	Theoretically predicted UV-visible absorption spectra of BPP and BPP(NHC) systems.	37
Figure-2.9.	Energy profile diagram for BPP , BPP(NHR) , and BPP(NHC) systems.	37
Figure-2.10.	¹ H NMR spectra (a) BPP and (b) BPP in the presence of a trace amount of TFA in DMSO-d ₆ .	37
Figure-2.11.	Comparative ¹ H NMR spectra for BPP and its TFA adduct.	38
Figure-2.12.	Visual color changes BPP -coated paper strips upon adding 0-100 ppm concentrations of TFA.	39
Figure-2.13.	Visual color change of BPP doped paper test strips of BPP upon exposing TFA vapor and its reversibility in the presence of TEA.	39
Figure-2.14.	(a) Reversible UV-visible spectra of BPP -TFA with TEA and (b) BPP -AcOH with TEA, respectively.	40
Figure-2.15.	Visual color change of acidified BPP system upon the addition of TEA in ACN.	40
Figure-2.16.	(Top) Column diagram of the absorbance at 552 (green columns) and 404 (orange columns) nm. The black line represents the ON-OFF threshold, and (Bottom) The dual-output combinatorial logic gates INH/IMP represent the two-state molecular switch operated in the ACN solution.	41
Figure-3.1.	¹ H NMR spectrum of NIMO in DMSO-d ₆ .	51
Figure-3.2.	¹³ C NMR spectrum of NIMO in DMSO-d ₆ .	52
Figure-3.3.	IR spectra of NIMO .	52
Figure-3.4.	High-resolution mass spectra of NIMO (m/z= 293.0922).	53
Figure-3.5.	(a) UV-visible absorbance spectra of a NIMO (33.7 μM) in ACN with different anions and (b) Bar diagram showing the	54

	alteration of relative absorbance of NIMO at 522 nm after adding other anions (A_0 : absorbance of the NIMO solution absence of any anions).	
Figure-3.6.	Visual color changes of NIMO up on gradual addition of F^- ions (0–2.6 equiv.) anions (naked eye view).	54
Figure-3.7.	Visual color changes of NIMO solution in ACN upon addition of 1.6 equiv. of each anion (naked eye view).	54
Figure-3.8.	(a) Increasing the absorbance of NIMO at 522 nm with the gradual addition of F^- ions (0–2.6 equiv., 0.2 equiv. intervals) at 25 °C; (inset: UV-visible spectrum of the NIMO) (b) Changes in UV-visible absorption spectra with increasing the F^- ions concentration (c) LOD of F^- to NIMO solution (d) UV-visible spectra of the NIMO with 0-2.6 equiv. of AcO^- ion in ACN.	55
Figure-3.9.	Interaction motif of NIMO with F^- ions (a) Job's plot for the Estimation of interaction stoichiometry of NIMO and F^- ions (b) B–H plot for the Estimation of interaction affinity of NIMO and F^- ions.	56
Figure-3.10.	Partial 1H NMR titration spectra of NIMO with F^- ions (0, 1, 2, 3, excess equiv.) in $DMSO-d_6$.	56
Figure-3.11.	The specific electronic transitions in the UV-visible spectrum of NIMO(OH) and NIMO(O⁻) are shown here, along with the specific FMOs.	59
Figure-3.12.	The CAM-B3LYP optimized geometries of NIMO(OH) , NIMO(O⁻) , and NIMO---X⁻ (X= F, Cl, Br, I, NO_3 , and OAc) are shown here, along with O-H distance and H---X ⁻ distances in Å Unit.	59
Figure-3.13.	Photograph of the prepared test paper strips and their color changes upon adding various concentrations of F^- ions.	60
Figure-3.14.	RGB color responses of NIMO for quantifying F^- ions.	61
Figure-3.15.	(a) Reversibility of the UV-visible spectra of NIMO + 2.6 equiv. of F^- ions upon adding HSO_4^- ions and (b) Color changes of a 33.7 μM ACN solution of NIMO . (Black line-	62

	NIMO , red line- NIMO + 2.6 equiv. of F ⁻ ions and blue line- NIMO +2.6 equiv. of F ⁻ ions + 2.6 equiv. HSO ₄ ⁻ ions).	
Figure-3.16.	A schematic representation of a complementary output INH and IMP logic circuit.	63
Figure-4.1.	¹ H NMR spectrum of HID in DMSO-d ₆ .	71
Figure-4.2.	¹³ C NMR spectrum of HID in DMSO-d ₆ .	72
Figure-4.3.	FT-IR spectrum of HID .	72
Figure-4.4.	HR-MS spectrum of HID .	73
Figure-4.5.	(a) UV-visible absorption and photoluminescence spectra of HID in DMSO. The emission intensity and highest wavelength absorption value are normalized for easier comparison. λ _{exc.} = 350 nm and (b) Photoluminescence lifetime decay profile of our HID in DMSO. λ _{exc.} = 375 nm and λ _{em.} = 475 nm.	76
Figure-4.6.	The specific electronic transitions in (a) the UV-visible spectrum of HID are shown here, along with (b) the specific FMOs.	76
Figure-4.7.	UV-visible absorption spectra of HID , HID -Al ³⁺ complex, and 4-AP in DMSO. For easier comparison, the wavelength absorbance values are normalized.	76
Figure-4.8.	The UV-visible titration spectra of HID (30 μM) in the presence of different concentrations of Al ³⁺ ions (0.0–10 equiv.) in H ₂ O/DMSO (9:1, V/V).	78
Figure-4.9.	(a) The specific electronic transitions in the UV-visible absorption spectrum of HID -Al ³⁺ complex with the specific FMOs and (b) theoretically predicted the UV-visible absorption spectrum of HID and HID -Al ³⁺ complex.	78
Figure-4.10.	(a) Photoluminescence titration spectra of HID (30 μM) in H ₂ O/DMSO (9:1, V/V), λ _{exc.} = 365, (excitation and emission slits are 5 nm and 5 nm respectively) in the attendance of different concentrations of Al ³⁺ ions (0–10 equiv.) and the corresponding change of emission intensity vs. [Al ³⁺] at 485nm upon steady addition of Al ³⁺ ions (inset) (b) Color	79

- chromaticity diagram for bare **HID** and **HID-Al³⁺** complex and (c) Visual colorimetric change of **HID** and **HID-Al³⁺** complex solution observed by the naked eye under a 365 nm UV lamp irradiation.
- Figure-4.11.** Photoluminescence spectra of **HID** with the gradual addition of Al³⁺ ions and its corresponding CIE diagram in (a, b) ethanol/H₂O (9:1, V/V) and (c, d) acetonitrile /H₂O (9:1, V/V). **81**
- Figure-4.12.** Visual colorimetric changes of solution of **HID** H₂O/DMSO (9:1, V/V) in the presence of various metal ions observed by the naked eye under a 365 nm UV-light irradiation. **81**
- Figure-4.13.** (a) Fluorescence spectra of **HID** (30 μM) in H₂O/DMSO (9:1, V/V) in the presence of various metal ions (10 equiv.) (b) Competitive selectivity of **HID** (30 μM) to Al³⁺ (10 equiv.) in the existence of other metal ions (1:10 ratio) and (c) Interference of different anions (10 equiv.) on the detection of Al³⁺ ions by **HID** (30 μM) in H₂O/DMSO (9:1 V/V), λ_{exc.} = 365 nm and λ_{em.} = 485 nm. **82**
- Figure-4.14.** (a) Job's plot for the Estimation of the binding stoichiometry of **HID** with Al³⁺ ions in H₂O/DMSO (9:1 V/V). Emission intensity at 485 nm is plotted against the molar ratio of [Al³⁺] / [Al³⁺] + [**HID**] (b) Partial ¹H NMR titration spectra of **HID** in the presence of Al³⁺ ions in DMSO-d₆ and (c) B-H plot of **HID-Al³⁺** complex for the Determination of binding constant. **82**
- Figure-4.15.** Time-resolved fluorescence lifetime decay profile of bare **HID** and **HID** in the presence of different concentrations of Al³⁺ ions in pure DMSO. λ_{exc.} = 375 nm and λ_{em.} = 475 nm. **83**
- Figure-4.16.** Calibration curve for the Estimation of the detection limit of Al³⁺ ions by employing our **HID** in (a) DMSO, (b) ethanol, and (c) ACN. **83**
- Figure-4.17.** Change of emission intensity of **HID** and **HID-Al³⁺** complex with the variation of pH. **86**

- Figure-4.18.** (a) Photoluminescence intensity change of **HID**-Al³⁺ complex solution due to the gradual addition of PA into the H₂O/DMSO (9:1, V/V) solution at $\lambda_{exc.} = 365$ nm and $\lambda_{em.} = 485$ nm (b) The bar graphs demonstrate the change of photoluminescence intensity of **HID**-Al³⁺ complex in the attendance of various NACs at $\lambda_{em.} = 485$ nm (c) Visual colorimetric change of **HID** and **HID**-Al³⁺ complex in the presence of Al³⁺ ions and PA by the naked eye under a 365 nm UV light illumination and (d) Paper strip method for the detection of PA by quenching of fluorescence of **HID**-Al³⁺ complex. **87**
- Figure-4.19.** Photoluminescence intensity changes of the **HID**-Al³⁺ complex solution and four equivalents of PA upon the addition of 10 equiv. of other competing NACs. **87**
- Figure-4.20.** (a) Job's plot for the Determination of interaction stoichiometry of **HID**-Al³⁺ complex with PA (b) B-H plot for the finding of interaction affinity of PA with **HID**-Al³⁺ complex and (c) the plot of fluorescence intensity of **HID**-Al³⁺ complex against log [PA] for finding out the detection limit **88**
- Figure-4.21.** S-V plots of the quenching of **HID**-Al³⁺ complex on interaction with PA as quenchers for finding the (a) static quenching and (b) dynamic quenching constants. **88**
- Figure-4.22.** Visual colorimetric change of paper strips-based test kit by the naked under a 365 nm UV light irradiation for the selective detection of Al³⁺ ions. Green color strips indicate the Al³⁺ ions; other metal ions do not show any visual colorimetric change under a 365 nm UV light irradiation. **90**
- Figure-4.23.** (a) Photoluminescence output of **HID** in the attendance of Al³⁺ ions and PA as chemically encoded inputs (b) The truth table and the relevant representative illustration of the **INH** logic gate operator. **90**

Figure-4.24.	Representing the viability of HADF cells after 24-, 48-, and 72-hour incubation with 20 μM HID .	91
Figure-4.25.	(a) Fluorescence microscopy image of HADF cells after 10 min due to the incubation of 10 μM HID in DMSO (b) after 10 min due to the incubation of 10 μM HID in addition to 30 μM Al^{3+} ions and (c) further introduction of 30 μM PA and incubation with HADF cells.	91
Figure-5.1.	^1H NMR spectrum of PbIL .	103
Figure-5.2.	^{13}C NMR spectrum of PbIL .	103
Figure-5.3.	^{31}P NMR spectrum of PbIL .	104
Figure-5.4.	HRMS spectra of PbIL ; (A) positive ion mode and (B) negative ion mode.	104
Figure-5.5.	FTIR spectra of pyrene butyric acid [PBA] (bottom) and PbIL (top); Circle-characteristic C-H stretching confirms the formation of PbIL .	105
Figure-5.6.	DSC trace of PbIL ionic salt under nitrogen atmosphere. The scanning rate is 2 $^{\circ}\text{C min}^{-1}$.	105
Figure-5.7.	(a) Excitation and emission spectra of the neat PbIL (inset: UV-visible spectra of neat PbIL) (b) the photograph of the neat PbIL under the naked eye (left) and (right) under a 365 nm UV lamp and (c) Corresponding CIE diagram for the neat PbIL (x=0.1475, y=0.3076).	107
Figure-5.8.	Visibility of letter NBU written with neat PbIL under (a, c) daylight and (b, d) a 365 nm UV lamp illumination on the TLC plate and Whatman no-40 filter paper, respectively.	107
Figure-5.9.	(a) DLS spectrum, (b) SEM images of the fabricated nPbIL , and (c) DSC trace of nPbIL under nitrogen atmosphere. The scanning rate is 2 $^{\circ}\text{C min}^{-1}$.	108
Figure-5.10.	(a) UV-visible spectra of Gumbos and nano-Gumbos PbI normalized form, (b) Emission spectra of the nano-Gumbos nl in different concentrations of PbIL and (c) Excitation and emission spectra of the nPbIL (inset: UV-visible spectra of neat PbIL).	109

- Figure-5.11.** (a) Photoluminescence titration spectra of **nPbIL** where $\lambda_{exc.} = 330$ nm (excitation and emission slits are 5 nm and 5 nm, respectively) in the attendance of different concentrations of PA (0–4.7 nM) in water (b) The CIE diagram for **nPbIL** and **nPbIL** in the presence of PA (c) Corresponding changes of emission intensities at 380 nm and 480 nm, respectively, due to the addition of PA in the water-suspended **nPbIL** solution and (d) ratiometric calibration plot of [PA] vs. (I_{380}/I_{480}) for the quantification of unknown concentration of PA with minimal error. **110**
- Figure-5.12.** (a) Emission spectra of the nano-Gumbos **nPbIL** and its equimolar solutions with a diverse nitro explosive (b) Photographs of the nano-Gumbos **nPbIL** with various nitro explosives under a UV lamp at 365 nm (c) Fluorescence response to the different nitro explosives of the nano-Gumbos **nPbIL** and (d) Interference studies of different kinds of nitro explosives in the presence of the nano-Gumbos **nPbIL-PA** framework at 380 nm. **111**
- Figure-5.13.** Calibration curve for the Estimation of LOD in the detection of PA employing our GUMBOS-based nanosensor. **112**
- Figure-5.14.** (a) The colorimetric changes of the paper-strips-based test kit in detecting PA in the aqueous solution with other nitro-explosives having the same concentrations under a 365 nm UV light exposure (b) displays the colorimetric change test kit in the various concentrations of PA under a portable 365 nm UV lamp and (c) the colorimetric changes of TLC plate as test kit in detecting PA under the exposure of 365 nm UV lamp. **114**
- Figure-5.15.** (a) Change of photoluminescence intensity of neat **PbIL** in the presence of PA under the excitation wavelength at 365 nm and (b) Bar diagram displays the change of emission intensity of neat **PbIL** and **PbIL** in the presence of PA. **116**

- Figure-5.16.** (a) Visible colorimetric photoluminescence behavior of neat **PbIL**-loaded filter paper (b) colorimetric change of neat **PbIL**-loaded filter paper on roughing with PA (c) it reverses after washing with DCM and (d) Change of photoluminescence intensity of neat **PbIL**-loaded filter paper after treatment with PA and its reverse after washing with DCM. **116**
- Figure-5.17.** (a) Visible colorimetric photoluminescence behavior of neat **PbIL**-loaded TLC plate, (b) colorimetric change of neat **PbIL**-loaded TLC plate on roughing with PA, and (c) it reverses after washing with DCM. **116**
- Figure-6.1.** ^1H NMR spectrum of **AMA** in DMSO-d_6 . **125**
- Figure-6.2** ^{13}C NMR spectrum of **AMA** in DMSO-d_6 . **125**
- Figure-6.3.** High-resolution mass spectra of our synthesized **AMA**. **126**
- Figure-6.4.** (a) The UV-visible absorption titration spectra recorded for a 6.54×10^{-5} M solution of **AMA** in DMSO with the gradual addition of DCP (0 to 2 equivalents) (b) The absorption spectra of **AMA** solution due to the introduction of other hazardous analytes (c) Changes in the absorbance values of **AMA** solution at 412 nm and 424 nm, respectively, are in the presence of DCP (0 to 2 equivalents) and (d) ratiometric calibration plot of $[\text{DCP}]$ vs. $\log(A_{412}/A_{424})$ to quantify the unknown concentration of DCP with the minimal experimental error. **127**
- Figure-6.5.** (a) Photoluminescence titration spectra of **AMA** (6.54×10^{-5} M) with a steady accumulation of DCP (0 equiv.-2 equiv.) in DMSO and (b) Displays the CIE diagram for the non-phosphorylated **AMA** and phosphorylated **AMA-DCP** products. **128**
- Figure-6.6.** (a) Emission intensity change due to the steady accumulation of various analogous toxic hazardous analytes (b) The bar diagram illustrates the variation in emission intensity at 440 nm, indicating the high selectivity of **AMA** towards DCP **129**

compared to other hazardous analytes under the same experimental conditions and (c) the probe **AMA**'s selectivity towards OPs and IPs is visually demonstrated under a 365 nm UV lamp irradiation.

- Figure-6.7.** Partial ¹H-NMR titration spectra of **AMA** with the steady accumulation of DCP in DMSO-d₆. **129**
- Figure-6.8.** Photoluminescence reversible spectra of phosphorylated **AMA** solution with the steady inclusion of TEA. **131**
- Figure-6.9.** The emission intensity response curve is used to determine the LOD of DCP. **131**
- Figure-6.10.** The colorimetric changes of **AMA**-doped filter paper were observed in two scenarios: (a) in the presence of numerous hazardous analytes and (b) under the exposure of various concentrations of DCP, under a 365 nm UV lamp irradiation. **131**
- Figure-6.11.** (a) Photoluminescence reversible spectra of phosphorylated **AMA** solution with the steady inclusion of TEA (b) Change of [TEA] vs. emission intensity at 440 nm when we gradually added TEA and (c) Change of fluorescence intensity of probe **AMA** due to the alternative addition of DCP and TEA, respectively. **133**
- Figure-6.12.** The emission intensity response curve is used to determine the LOD of DCP. **134**
- Figure-6.13.** The colorimetric changes of **AMA**-doped filter paper were observed in two scenarios:(a) in the presence of numerous hazardous analytes and (b) under the exposure of (10⁻³ -10² ppm) concentrations of DCP, under a 365 nm UV lamp irradiation. **136**
- Figure-6.14.** Fluorescence responses of fabricated **AMA**-dipped filter paper toward detecting (A) DCP vapor, (a) **AMA**, (b) DCNP, (c) DCP, (d) DMMP, (e) TIMEP, (f) TMP, (g) NaH₂PO₄, (h) TEP, (i) Na₂HPO₄, (j) HCl, (k) CH₃COOH, (l) T2CP, (m) BA, (n) MCE, (o) BB, (p) 2CPS, (q) Na₃PO₄, (r) 2CES, (s) TA, respectively, (B) at various concentrations of DCP vapor, and **136**

(C) **AMA** solution in contact with DCP vapor under the exposure of a 365 nm UV lamp.

List of tables

Tables	Page No.
Table-2.1. The truth table for combinatorial INH and IMP logic gates. Inputs: the presence of acid and base in the ACN solution of BPP . Outputs: absorbance at 404 nm and 552 nm (high absorbance: 1; low absorbance: 0)	41
Table-3.1. CAM-B3LYP computed structural parameters extracted from optimized geometries of NIMO and NIMO---X⁻ (X = F, Cl, Br, I, NO ₃ , and OAc) complexes are shown here, along with the Mulliken charge	59
Table-4.1. Spectral data of HID 's emission and absorption in various solvents, in nm.	74
Table-4.2. Changes in fluorescence quantum yield of HID in the presence and absence of Al ³⁺ ions and PA.	81
Table-4.3. Time-resolved photoluminescence decay parameters and the average photoluminescence lifetime of HID in the absence and attendance of Al ³⁺ ions	81
Table-4.4. Comparison of different Al ³⁺ ions chemosensors and their specifications.	84
Table-4.5. Comparison with the detection limits of sensing PA by various sensors.	88
Table-5.1. Comparison with the detection limits of sensing PA by various sensors	112
Table-6.1. Comparison table of various chemosensors that have been introduced for detecting nerve agent stimulants in the last few decades with our probe AMA	136

List of appendices

Appendix	Page No.
List of publications	143-144
List of seminars/conferences/workshops attended	145